


# Failure cause assessment of steam reformer radiant tube after long-term service

Anna N. Dobrotvorskaia  | Mstislav A. Dobrotvorskii | Elena P. Shevyakova | Michail A. Simanov

CJSC “NPO”Lencor”, St. Petersburg, Russia

## Correspondence

Anna N. Dobrotvorskaia, CJSC  
“NPO”Lencor”, St. Petersburg 190000,  
Russia.  
Email: [adobrotvorskaja@npo-lencor.ru](mailto:adobrotvorskaja@npo-lencor.ru)

## Abstract

This study investigates the damage, microstructure, and mechanical evolution of service-exposed HP40NbTi radiant tubes of a steam reformer furnace. Tube failure was reported after 6-year of working at 525°C–830°C in the form of visible longitudinal and transverse cracks. The microstructure was evaluated using optical and scanning electron microscopy equipped with energy-dispersive X-ray spectrum analysis. The carbide phase transformation was determined by the method based on the matrix dissolution technique and X-ray diffraction. The results of this study showed that the primary cause of the longitudinal crack formation is the local overheating and the oxidation of the dendritic grain boundaries. The  $M_7C_3$  carbide transforms completely into the metastable  $M_{23}C_6$  phase during high-temperature service. Metallographic examinations revealed the shrinkage cavities and creep voids that are nucleated on both Cr- and Nb-carbides. The continuous oxide layers of  $Cr_2O_3$  and  $SiO_2$  formed near the inner and outer tube surfaces and the matrix's chemical composition near the outer tube surface was found to be depleted of Cr and C. Mechanical properties are irregular across the samples. A little margin of safety is noted, while the complete ductility dip is detected at room temperature. The root cause analysis of the failure under investigation showed that the tube failed due to the creep.

## KEYWORDS

carbides, centrifugally cast steel furnace tubes, creep rupture, failure analysis, material degradation, microstructural observation, phase transformation, reformer furnace tube

## 1 | INTRODUCTION

Steam reformer radiant tubes (catalytic conversion of methane with steam) are the key components in the production of technical hydrogen, which has been widely used in the ammonia industry for about half a century,<sup>[1,2]</sup> and also in the petroleum industry in the past decades, owing to the development of the deep oil-refining processes.<sup>[3]</sup> Many experiments in the areas of engineering and operation of steam

reformer furnaces were carried out including those concerned with their main component—reformer furnace tube. Numerous data on the residual life of reformer tubes and sources of their rupture after service exposure have been collected.<sup>[4–6]</sup>

The key question in the engineering and production of steam reformer tubes is the choice of the tube material, which determines their service life. Heat-resistant Fe-Cr-Ni-alloys of H-type (HK, HT, and HP) are widely

used.<sup>[1,7–9]</sup> Modern HP alloys of the third generation have a complex chemical composition and contain (wt.%): 0.3–0.6 C, 15–35 Cr, 20–45 Ni, Si, Mo, W, Mn, Ti, Nb, rare-earth elements, and balance Fe. The alloy structure is multiphase and consists of the supersaturated solid solution  $\gamma$ -Fe-Cr-Ni, as well as chromium and niobium carbides ( $\text{Cr}_m\text{C}_n$  и  $\text{Nb}_m\text{C}_n$ ).<sup>[9,10]</sup> During high-temperature service, the carbides continuously transform, which results in changes in the mechanical characteristics.<sup>[11]</sup>

Material choice is conditioned by the demanding requirements for equipment due to the possible risks of accidents under high temperatures and specifics of the manufacturing process. In steam reformer facilities, the service conditions of structural materials are extreme: radiant tubes are exposed simultaneously to high temperature, corrosive environment, and external stress. Under such conditions, the structural material should have high mechanical strength, be heat resistant, creep resistant, high-temperature embrittlement resistant, resistant to chromium carbide deposition, and possess carbide stabilization properties.

During many years of steam reformer furnace exploitation, a large amount of information about their failure and depressurization causes was collected.<sup>[3,4,12–15]</sup> For a considerable length of service time, the dominant modes are usually destruction in the creep process, embrittlement as a result of carbon diffusion (cementation), as well as destruction due to technological factors, in particular as a result of local pipe overheating. Premature failures of steam reformer furnace facilities can lead to expensive and tragic consequences.

Damage to the radiant tubes is often a result of microstructural degradation of as-cast material after long-term service exposure. This study investigates the microstructural

and mechanical evolutions, oxidation process behavior for HP40NbTi radiant tubes after 6-year service exposure.

## 2 | MATERIALS AND METHODS

After a 6-year service, several service-exposed and overheated radiant tubes were replaced to determine the microstructural and mechanical degradation. These tubes were operated at high temperature (525–830°C) in a hydrogen production unit with a catalyst ReforMax 210 LDP (NiO,  $\text{K}_2\text{O}$ , and calcium aluminate) and ReforMax 330 LDP (NiO and calcium aluminate). The material studied is HP40NbTi centrifugally cast austenitic stainless alloy with chemical composition (wt.%) of 0.5 C, 26 Cr, 34 Ni, 0.8 Si, 1.3 Nb, 0.2 Ti, 0.03 Mo, 0.15 Mn, and balance Fe. The investigated specimens were prepared from three radiant tubes and schematically are shown on Figure 1. The first specimen is cut from the upper part of the tube within the destruction zone (denoted by red line on Figure 1) and is labeled as I-Specimen. The second and third ones were cut from the lower part of different service-exposed tubes away from the destruction zone and are labeled as II-Specimen and III-Specimen, respectively.

Fractography was performed on the fracture surface of failed Specimen-I. The microstructural observations were performed on the cross-section of tube material using an optical microscope Versamet with a Thixomet image analyzer. The investigated samples were etched in 4%  $\text{HNO}_3$  solution in  $\text{C}_2\text{H}_5\text{OH}$ . Furthermore, the TESCAN Mira-3 scanning electron microscopy (SEM) using backscattered electron and secondary electron (SE) modes was employed equipped with energy-dispersive and wave-dispersive X-ray spectrum analysis elements distribution of specimens (EDS) module to analyze the

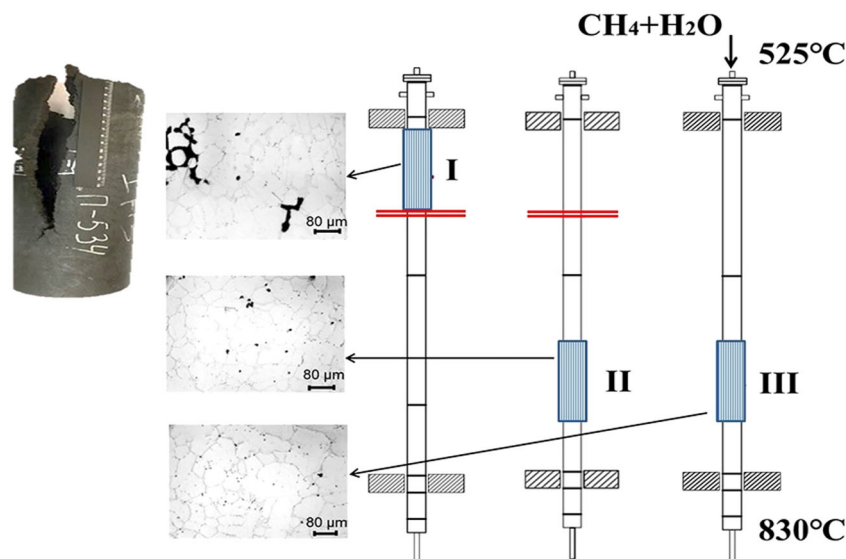


**FIGURE 1** Schematic representation of the radiant tubes, positions of the samples with the corresponding optical microscopy images, and the picture of the failure tube (Specimen-I) [Color figure can be viewed at [wileyonlinelibrary.com](http://wileyonlinelibrary.com)]

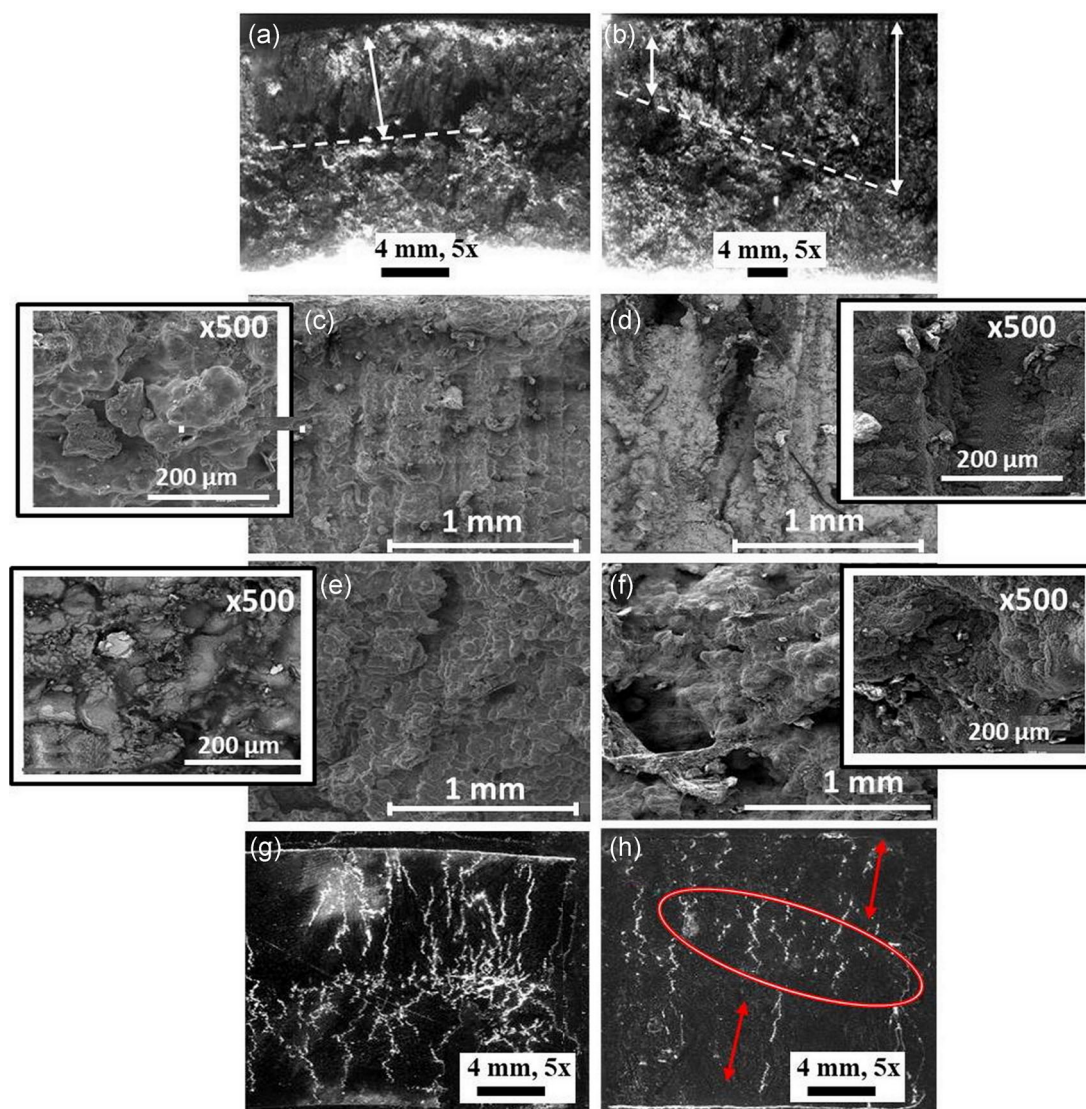


**FIGURE 2** Fractographic analysis of the failed Specimen-I in the area of the longitudinal (left-side pictures) and perpendicular (right-side picture) cracks. (a,b) Fracture surface; (c–f) scanning electron fractographs (secondary electron mode) accompanied with high magnification (small frames) in the region close to the outer tube surface (c,d) and in the crack opening region (e,f). (g,h) Metallographic images; the oval shows the tearing-off zone under torsion and the arrows indicate the tearing-off zone under tension [Color figure can be viewed at [wileyonlinelibrary.com](http://wileyonlinelibrary.com)]

compositions of carbides and precipitates. To characterize the carbide transformation after high-temperature material aging, the matrix dissolution technique was utilized. The electrolytic extraction of precipitates was carried out in 10% HCl + CH<sub>3</sub>OH solution at anodic current density 40–50 mA/cm<sup>2</sup> and  $T = -10^{\circ}\text{C}$  within a sufficient time to extract enough powder for X-ray diffraction (XRD) analysis. The XRD analysis was performed by Rigaku Ultima IV X-ray diffractometer equipped with X-ray powder diffraction software.

Hardness distribution was measured using Wilson hardness Rockwell tester. Tensile tests were performed by standard methods at both room (20°C) and service (840°C) temperatures, to determine the mechanical properties.

### 3 | RESULTS AND DISCUSSION

#### 3.1 | Fractographic study of fractures

Fractographic analysis was done for failed Specimen-I, shown as an image in Figure 1. As can be seen, visual cracks have propagated longitudinally, oriented along the pipe axis, and transversely, oriented in a perpendicular plane. Figure 2 illustrates the results of fractographic analysis in the area of the longitudinal (left-side pictures) and perpendicular (right-side picture) cracks. As shown in Figure 2a, the depth of the damaged metal relative to the outer surface is approximately uniform and equals 5(1) mm for the longitudinal crack. For perpendicular

crack, the damaged metal depth varies within 2(1)–10(1) mm, which indicates local damage of the tube (see Figure 2b).

To investigate the cracking modes, the Specimen-I surface was examined by SEM (SE mode). Figure 2c–f illustrates the SEM images of the failure surface at two different magnifications ( $\times 100$  and  $\times 500$ ). Analysis of the surface in the area of the longitudinal crack in Figure 2c,e revealed that the material damage close to the outer surface of the pipe body corresponds to the ductile intergranular deformation with the formation of a stone-like fracture (Figure 2c). In the crack opening region, the local dimples are observed on the fracture surface (see Figure 2e) and the fracture is characterized as quasi-brittle.

Near the transversal crack, there is no indication of molten metal that defines this rupture as secondary. The microstructural observations made at both magnifications show the quasi-brittle fracture surface (Figure 2d,f), which is most clearly seen close to the crack opening region (Figure 2f).

To clarify the probable causes of the crack appearing, a metallographic analysis was performed and resulted on Figure 2g,h. Two samples of tube surface were taken as follows: the pattern No. 1 is cut out at the place of the greatest longitudinal crack opening and the pattern No. 2 is done from the transversal crack fracture. The damaged metal assessment was carried out on nonetched patterns based on the qualitative judgment of the number and locations of the identified intergranular destruction traces. Figure 2g shows that the destruction traces density is located in a plane parallel to the outer surface of the tube body (the upper border of the figure). It is noteworthy that the density increases from the internal side. This indicates a relatively rapid crack opening at the outer surface of the tube and a slow one at the inner surface. For the pattern No. 2 (Figure 2h), the greatest damage was observed only on one side closer to the local destruction. On the image, the oval shows the tearing-off zone under torsion and the arrows indicate the tearing-off zone under tension. As cracks open under normally applied stresses, it is possible to suggest that the tube deformation was succeeded by bending or rotation. This suggestion is in agreement with the fractographic results.

The aforementioned results suggest that the metal destruction occurred in two stages. First, the cavity appeared with the subsequent opening of the longitudinal crack due to increased internal pressure of the service environment. The longitudinal crack is a ductility-dip cracking with the stone-like fracture surface near the outer tube surface. At the next region of crack opening, the fracture transformed into a quasi-brittle. The subsequent structure destruction is the result of the bending

deformation with the transverse crack appearing on the tube body with the quasi-brittle fracture surface.

## 3.2 | Phase transformations and microstructure changes

Figure 3 illustrates the optical (left row) and scanning electron (right row) microscopy of the central area of Specimen-I (Figure 3a,b), Specimen-II (Figure 3c,d), and Specimen-III (Figure 3e,f). The small frame pictures for optical microscopy images are run with higher magnifications. It can be seen that the microstructure of all studied specimens consists of an austenitic matrix and a continuous network of eutectic carbides, marked by dark and white colors on SEM images. Figure 3 also demonstrates the precipitations of many small dispersive particles located near the dendritic boundaries and the microporosity resulted from interdendritic shrinkage during alloy crystallization. The shrinkage porosity is one of the main problems in the centrifugal casting of long empty thick-walled cast blocks.<sup>[16]</sup>

Elements distribution of specimens was measured by EDS mapping and resulted in Figure 4. EDS analysis reveals that the eutectic phase is a mixture of chromium (dark phase) and niobium-titanium (NbTi)C (white phase) carbides. XRD analysis of the particles extracted from the studied specimens shows that the main carbide is  $M_{23}C_6$  (M mostly is Cr) and the volume fraction of (NbTi)C is too low to be detected, as shown in Figure 5. Diffraction analysis of the  $M_{23}C_6$  carbide presents this phase has an FCC structure with a lattice parameter of 1065 nm.

Figure 5 depicts the XRD analysis of extracted carbide phase for Specimen-II. In addition, signals identified as phases of  $SiO_2$ ,  $Cr_2O_3$ , and mixed-valent  $Fe_2O_3$  are observed. The presence of the  $Cr_2O_3$  signal is probably explained by the penetration of oxide particles from the studied specimen into the carbide phase without compound changing since chromium (III) oxide is acid-resistant and slightly interacts with a dilute solution of inorganic acids.<sup>[17]</sup> The presence of the  $SiO_2$  phase might be due to its formation during the oxidation of elemental silicon on the sample surface at anodic dissolution. At the same time, the  $SiO_2$  formation in oxidation processes during the facility exploitation is possible and its subsequent entry into the carbide phase. It is suggested indirectly by the EDS results, as will be shown in Figure 6. Similar results were obtained in Song.<sup>[13]</sup> The signals corresponding to  $Fe_2O_3$  can be explained by the aerobic oxidation of highly dispersed reactive particles of the iron-containing carbide phase during the rinsing of the extracted sample or their storage at high humidity.



**FIGURE 3** Microstructure of the Specimen-I (a,b), Specimen-II (c,d), and Specimen-III (e,f): left-side pictures— $\times 100$  optical microscopy images ( $\times 400$  in frame); right-side picture—scanning electron microscopic images (backscattered electron mode) [Color figure can be viewed at [wileyonlinelibrary.com](http://wileyonlinelibrary.com)]

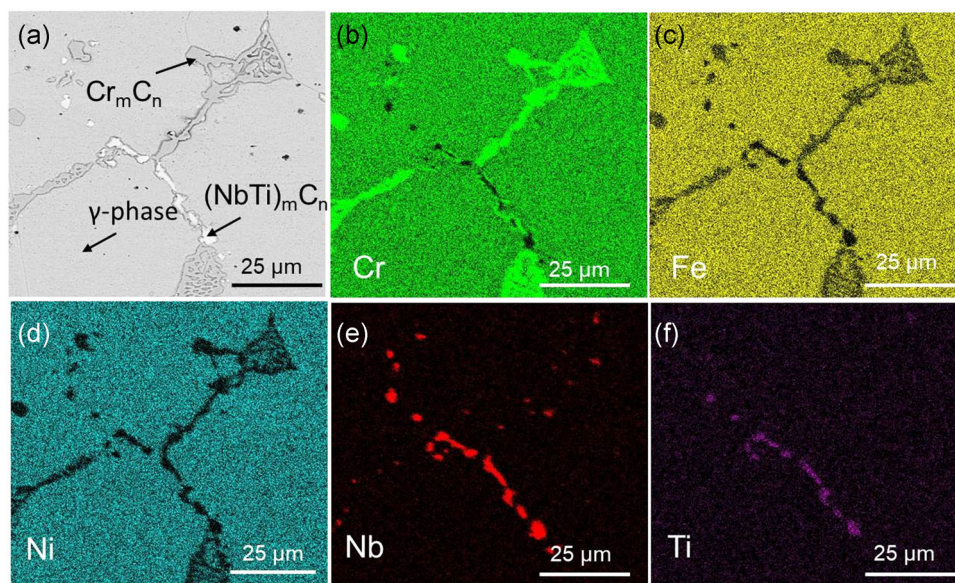
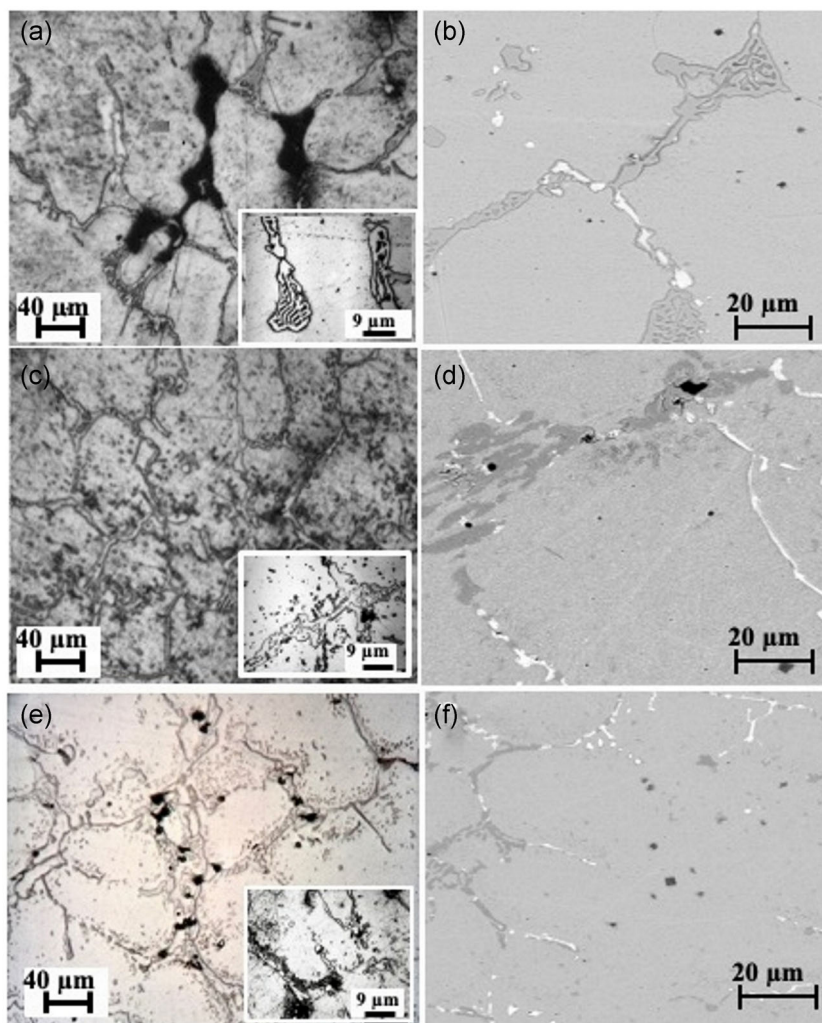


**FIGURE 4** EDS mapping of the elemental distribution (b–f) of the Specimen-I in the central surface area. (a) Scanning electron microscopic image (backscattered electron mode). EDS, elements distribution of specimens [Color figure can be viewed at [wileyonlinelibrary.com](http://wileyonlinelibrary.com)]

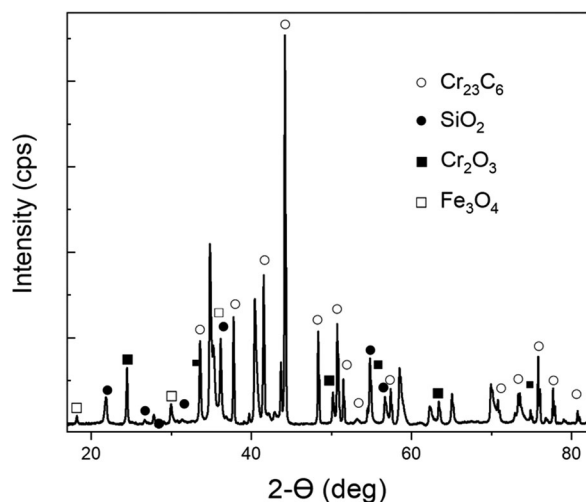


**FIGURE 5** X-ray diffraction analysis of extracted carbide phase for the Specimen-II. It is noteworthy that  $\text{SiO}_2$  and  $\text{Cr}_2\text{O}_3$  are the results of internal oxidation;  $\text{Fe}_2\text{O}_3$  is the result of the inadequate rinsing of the extracted sample

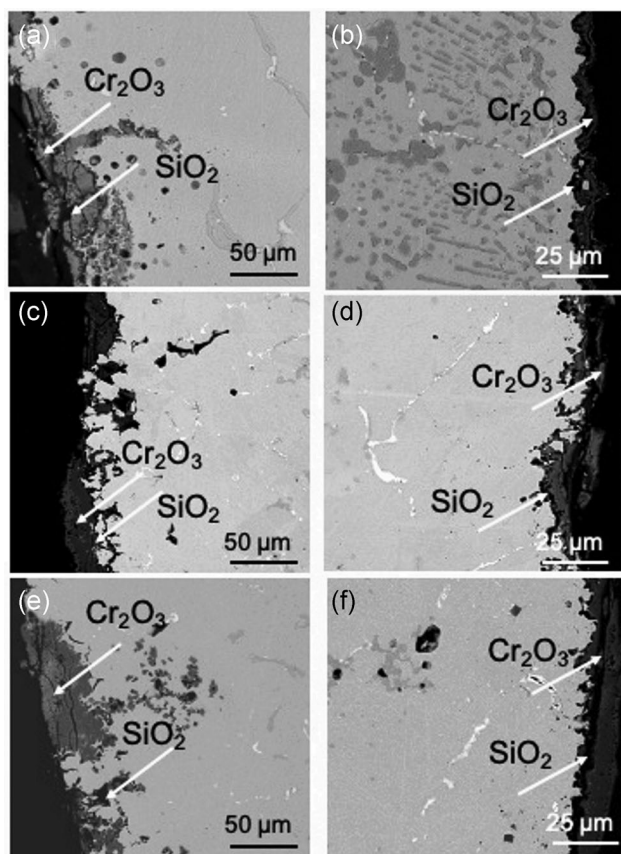


**FIGURE 6** Scanning electron microscopic images (backscattered electron mode) of the specimens near the outer (left-side pictures) and inner (right-side pictures) tube's surfaces: (a,b) Specimen-I; (c,d) Specimen-II; (e,f) Specimen-III

It is known from the literature that at high-temperature exploitation of cast alloys, there is a continuous transformation of the carbide phase in the microstructure.<sup>[11]</sup> The carbide transformation corresponds to the change in the carbide phase-type and the formation of transitional inter-metallic compounds.<sup>[11,18]</sup> The primary eutectic none-equilibrium  $\text{M}_7\text{C}_3$  carbide transforms into more stable  $\text{M}_{23}\text{C}_6$  carbide and  $(\text{FeCrNi})_m\text{C}_n$  to  $\text{M}_{23}\text{C}_6$ .<sup>[13]</sup> According to previous studies,<sup>[9]</sup> the metastable  $\text{NbC}$  phase would transform into G phase ( $\text{Ni}_{16}\text{Nb}_6\text{Si}_7$ ) at a certain range of temperature (700–1000°C). However, this transformation was not observed for studied specimens.

As discussed above, the main result of the carbide transformation is an increase of the total carbide phase volume in the metal structure. The reason for this is that the carbon concentration decreases in the final carbide phase. The corresponding increase of the metallic element concentration in the carbide phase is due to this element diffusion from the matrix  $\gamma$ -phase. Expelled C atoms from the transformation of  $\text{M}_7\text{C}_3$  to  $\text{M}_{23}\text{C}_6$  promote the appearance of the small dispersive  $\text{M}_{23}\text{C}_6$  precipitation phase. It is noteworthy that the small, unstable  $\text{M}_{23}\text{C}_6$  particles tend to coarsen into blocky carbide during long-time high-temperature exposure (Figure 5).

The microstructure image in Figure 3 shows a lot of voids in contact with the blocky Cr-rich  $\text{M}_{23}\text{C}_6$  and Nb-rich carbides that indicate the creep development. The mechanism of the creep-induced embrittlement is linked to the generation and coalescence of intergranular voids with the formation of large cavities near the precipitates.<sup>[19]</sup> During the material exploitation at high temperature, the creep voids evolve into micro- and then macrocracks.<sup>[3]</sup> The cavities around precipitates are formed due to the alloying element diffusion at the eutectic carbide/matrix and dispersive precipitate/matrix interfaces.

Coarse carbides enriched by Cr and Nb can be nucleators of voids in the material during the creep process.<sup>[3]</sup> This study suggests that the creep voids are nucleated on both Cr- and Nb-carbides, as shown in Figure 3. Carbide coalescence and coarsening mechanisms are diffusion-dependent. Even a slight increase of service temperature can significantly affect the kinetics of particle growth and thus accelerate the nucleation of creep voids.<sup>[20,21]</sup> Therefore, the service temperature is the key factor influencing the equipment lifetime at high-temperature exposure with an aggressive environment.

### 3.3 | Oxidation processes on the tube's inner and outer surfaces

The radiant tubes were exposed to the oxidation environment at a high temperature. The SEM images



of the specimens near the outer (left row) and inner (right row) tube's surfaces are presented in Figure 6. The element distribution was measured using EDS mapping analysis. It can be seen that the continuous chromium-rich oxide layer and the fragmental silicon-rich oxide layer formed on the inner and outer tube surfaces. These oxides are  $\text{Cr}_2\text{O}_3$  and  $\text{SiO}_2$ ,<sup>[13]</sup> which supported the XRD results presented in Figure 5. Figure 7 illustrates in more detail the element distribution map for the Specimen-III. As shown, the matrix near the inner and outer tube surface layer is depleted of Cr due to the formation of the oxides. Near the outer tube surface, the Al particles from the destroyed catalyst and TiN particles are observed. The high-temperature corrosion had led to inner and outer surface decarburization and the subsurface regions free from precipitates are observed. Also, some creep voids appeared in this region normally formed at the original location of the dissolved carbides.

Similar morphologies of the inner and outer tube surfaces are observed for other specimens, as illustrated in Figure 6, except for the width of the decarburized region. For the failure Specimen-I, the narrower decarburized region (no more  $15\ \mu\text{m}$ ) is observed, beneath which the increased density of dispersed precipitates appeared that indicates the carburization of the inner tube surface.

### 3.4 | Mechanical properties

Figure 8 shows the comparison of the Brinell hardness between specimens for the center, inner, and outer surface regions. It can be seen that the hardness values are distributed uniformly, except the region near the outer tube surface where hardness for Specimen-I and -III decreases by  $\sim 10\%$ .

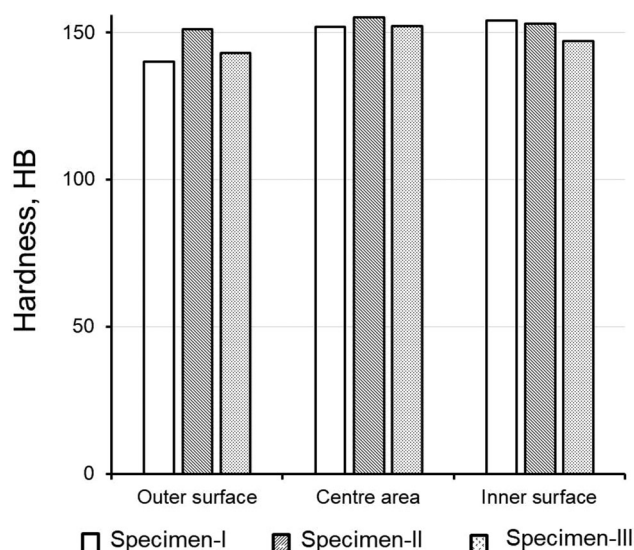


**FIGURE 8** Brinell hardness of the specimens for the center, inner-, and outer-surface regions

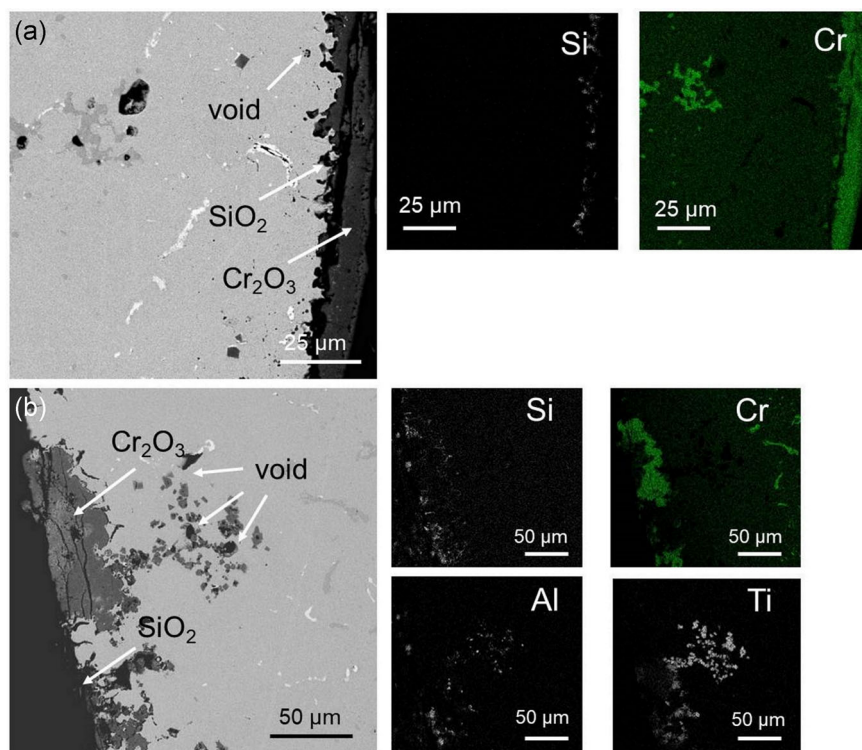


**FIGURE 7** Scanning electron microscopic images (backscattered electron mode) and the element distribution EDS map for the Specimen-III near the inner (a) and outer (b) tube's surfaces. EDS, elements distribution of specimens

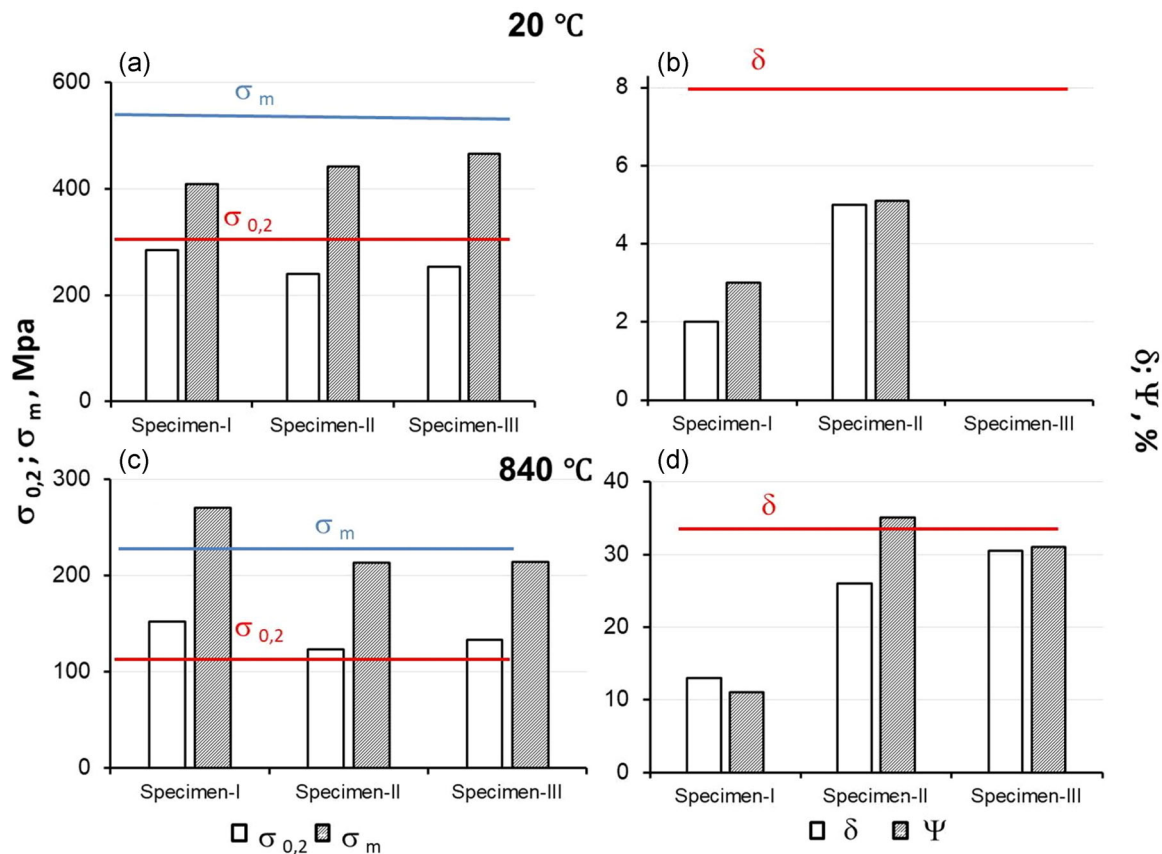


**FIGURE 9** Tensile properties of the studied tubes at 20°C (upper pictures) and 840°C (low pictures). The color lines depict the literature values for similar alloys. (a,c) Yield strength ( $\sigma_{0.2}$ ) and tensile strength ( $\sigma_m$ ) parameters; (b,d) residual elongation ( $\delta$ ) and residual constriction ( $\psi$ ) parameters [Color figure can be viewed at [wileyonlinelibrary.com](http://wileyonlinelibrary.com)]

Tensile properties of the studied tubes at room (upper pictures) and service (low pictures) temperatures are illustrated in Figure 9. The color lines depict the literature values for similar alloys.<sup>[22]</sup> It can be seen that the yield strength ( $\sigma_{0.2}$ ) and tensile strength ( $\sigma_m$ ) for specimens are comparable or slightly below the literature data for both temperatures, as shown in Figure 9a,c. The ductility properties, such as residual elongation ( $\delta$ ) and residual constriction ( $\psi$ ), are presented in Figure 9b,d for both temperatures. It is shown that for the service temperature the ductility for Specimen-I decreases remarkably while the ductility for Specimens-II and -III are in agreement with the literature, as shown in Figure 9d. Figure 9b presents the dramatic loss of ductility for room temperature. The samples of Specimen-III were destroyed during the tensile test. The ductility dip is due to the variations of the type, shape, and size of the precipitates and is the important factor. If the ductility is too low, the tube cannot be operated.

## 4 | CONCLUSIONS

Based on the results and analysis, several conclusions can be drawn as follows:

- (1) The primary cause of the longitudinal crack formation is the local overheating and the oxidation of the dendritic grain boundaries.
- (2) The microstructure of the serviced alloy corresponds to the structure of centrifugal cast chromium-nickel alloy and consists of austenite matrix ( $\gamma$ -phase) with chromium- and niobium-based eutectic carbides, as well as secondary dispersive precipitates enriched with chromium. The transformation of  $M_7C_3$  to  $M_{23}C_6$  carbides occurred completely during high-temperature service.
- (3) The shrinkage cavities and creep voids are observed along grain boundaries of the matrix/carbide phase. The creep voids are nucleated on both Cr- and Nb-carbides.



- (4) Near the inner and outer tube surfaces, the continuous oxide layer of  $\text{Cr}_2\text{O}_3$  and  $\text{SiO}_2$  is formed. Close to the outer tube surface, the matrix's chemical composition is depleted of Cr and C, also the traces of fragmented catalyst are found.
- (5) Irregularity of mechanical properties is observed. At service and room temperatures, there exists a small margin of safety. The ductility characteristics for specimens without the visible destruction zones are in agreement with literature data for service temperature while for failed specimens it is significantly decreased. For room temperature, the complete ductility dip for all studied specimens is detected.
- (6) The root cause analysis of the failure under investigation showed that the tube failed due to creep failure.

### CONFLICTS OF INTEREST

The authors declare no conflicts of interest.

### DATA AVAILABILITY STATEMENT

The data that support the findings of this study are available on request from the corresponding author. The data are not publicly available due to privacy or ethical restrictions.

### ORCID

Anna N. Dobrotvorskaja  <http://orcid.org/0000-0002-4489-8890>

### REFERENCES

- [1] M. Garbiak, W. Jasinski, B. Piekarski, *Arch. Foundry Eng.* **2011**, 11, 47.
- [2] M. Ojha, A. K. Dhiman, *Int. Rev. Chem. Eng.* **2010**, 6, 631.
- [3] A. Bahrami, P. Taheri, *Metals* **2019**, 9, 1026.
- [4] A. Alvino, D. Lega, F. Giacobbe, V. Mazzocchi, A. Rinaldi, *J. Eng. Failure Anal.* **2010**, 17, 1526.
- [5] E. Guglielmino, R. Pino, C. Servetto, A. Sili, *Handbook of Materials Failure Analysis with Case Studies from the Chemicals, Concrete and Power Industries*, Butterworth-Heinemann, Oxford **2016**.
- [6] J. Swaminathan, K. Guguloth, M. Gunjan, P. Roy, R. Gho, *Eng. Failure Anal.* **2008**, 15, 311.
- [7] J. R. Davis, *ASM Specialty Handbook. Heat-Resistant Materials*, ASM International, New York **1997**.
- [8] S. V. Afanasiev, S. Sergeev, A. Pyrkin, A. Afanasiev, *Expos. Oil Gas* **2016**, 47, 56.
- [9] de L. H. Almeida, A. F. Ribeiro, I. L. May, *Mater. Charact.* **2003**, 49, 219.
- [10] A. I. Rudskoy, A. S. Oryshchenko, S. Y. Kondratyev, G. P. Anastasiadi, M. D. Fuks, S. N. Pterov, *Metallovedeniye i termicheskaya obrabotka metallov* **2013**, 4(694), 42.
- [11] A. V. Ptashnik, S. Y. Kondratyev, G. P. Anastasiadi, S. N. Petrov, *Nauchno-tekhnicheskiye vedomosti SPbGPU* **2015**, 3, 40.
- [12] Z. Han, L. Cao, L. Wang, C. Du, X. Qian, G. Xie, *J. Mater. Eng. Performance* **2020**, 29, 5458.
- [13] R. W. Song, *J. Eng. Failure Anal.* **2018**, 88, 63.
- [14] M. Mostafaei, M. Shamanian, H. Purmohamad, M. Amini, A. Saatchi, *Eng. Failure Anal.* **2011**, 18, 164.
- [15] M. Whittaker, B. Wilshire, J. Brear, *Mater. Sci. Eng. A* **2013**, 580, 391.
- [16] M. Sahoo, S. Sahu, *Principles of Metal Casting*, McGraw-Hill Education, New York **2014**.
- [17] V. N. Alekseev, *The Course of Qualitative Chemical Semi-Microanalysis*, Chemistry, Moscow **1973**.
- [18] E. A. Kenik, P. J. Maziasz, R. W. Swindeman, J. Cervenka, D. May, *Script. Material.* **2003**, 49, 117.
- [19] D. Villanueva, F. Junior, R. L. Plaut, A. F. Padilha, *Mater. Sci. Technol.* **2006**, 22, 1098.
- [20] W. Z. Wang, F. Z. Xuan, Z. D. Wang, B. Wang, C. J. Liu, *Mater. Des.* **2011**, 32, 4010.
- [21] D. R. Jones, *Eng. Failure Anal.* **2004**, 11, 873.
- [22] ASTM B407-08AR19 *Standard Specification for Nickel-Iron-Chromium Alloy Seamless Pipe and Tube*, **2017**.

**How to cite this article:** A. N. Dobrotvorskaja, M. A. Dobrotvorskii, E. P. Shevyakova, M. A. Simanov, *Mater. Corros.* **2022**, 1–9.  
<https://doi.org/10.1002/maco.202213068>